Transcranial functional shear wave elastography

Master thesis TU Delft
XIN TAN
SUPERVISORS: DAVID MARESCA, RICK WAASDORP

[1]dept. Imaging Physics, Medical Imaging, Maresca Lab
Faculty of Mechanical, Maritime and Materials Engineering
Delft University of Technology
Delft, the Netherlands

ABSTRACT

Many functional imaging modalities such as EEG, fMRI, and fUS were developed, and have the potential to achieve the brain-computer interface. In addition to those conventional functional imaging modalities which measure the electrical signal or neurovascular coupling induced by brain activity, Patz et al. found evidence for the existence of a neuromechanical coupling that can be detected by elastography. This project proposes transcranial functional shear wave elastography (SWE) that images the elasticity of the human brain tissue with ultrasound noninvasively. To correct aberration induced by the skull, we introduce an aberration correction algorithm based on ray tracing which corrects the aberration for both shear wave generation and image readout. The result shows that the aberration correction can improve the SNR and contrast of shear wave images and help the reconstruction of elasticity of agar phantom which includes an aberrator and help SWE recover the elasticity of brain tissue through the aberrator such as skull. Although transcranial functional SWE still has weakness in spatial range of measurements, temporal resolution, and spatial resolution, it has the potential to be applied to BCI as the development of shear wave tracking technique and high frame rate ultrasound imaging.

INDEX TERMS
Transcranial functional Shear wave elastography; Aberration pushing correction; Aberration imaging correction; Brain-computer interface

I. INTRODUCTION

The brain controls the voluntary movements of skeletal muscles via specialised nerves. The combination of the nervous system and muscles, working together to permit movement, is known as the neuromuscular system. However patients with neuromuscular disorders such as amyotrophic lateral sclerosis have muscle weakness, atrophy, and muscle spasms throughout the body due to the degeneration of the upper motor and lower motor neurons. Individuals affected by the disorder may ultimately lose the ability to initiate and control all voluntary movement [1]. Brain-computer interfaces (BCI) can help neuromuscular disorders patients carry out the desired action by acquiring the brain signal, translating brain activity into a command that can be executed on a external devices, such as robotic prosthesis.

Many brain signals have been discovered that can be detected and used for BCI. In principle brain signals used for BCI can be categorized into electrical, magnetic, and metabolic signal. Electroencephalogram (EEG) [2] demonstrated to be able to detect the electrical signal and measure the mental activity. But EEG has limited spatial resolution and poorly measures activity below the cortex because of the signal attenuation and dispersion caused by the dura, skull, and scalp [3]. Some invasive modalities such as intracortical electrodes [4], and electrocorticography (ECoG) [5] also can measure the brain activities by acquiring electrical signals but require a surgery to implant, cause chronic brain tissue damage and face electrode degradation.

Metabolic signal particularly neurovascular coupling was recently widely studied for BCI. Functional magnetic resonance imaging (fMRI) measures blood oxygen level-dependent (BOLD) and correlate with neural activity. But, MRI systems are expensive, not portable, and most importantly neurovascular coupling is activated $\sim$2 seconds after neural activities which means there is few seconds latency between brain activity and brain signal readout by BCI. In 2011, Macé et al. [6] introduces functional ultrasound (fUS) imaging that is more affordable, more portable, and has better spatiotemporal resolution than fMRI. fUS measures transient changes in cerebral blood volume (CBV) where the neural activities occur [6]. However, like fMRI, fUS relies on CBV changes which are neurovascular coupling and have the same typical delay of about 2 seconds after neural activity [7], and the application of fUS in neuroscience is currently limited by

skull bones aberration and requires a craniotomy.

In 2019, Patz et al. [8] found evidence for the existence of a neuromechanical coupling, particularly elasticity change due to neural activity. Patz et al. measured the brain tissue elasticity decrease using functional magnetic resonance elastography (fMRE) after applying repetitive electric stimulation at different frequencies (0.1, 1 and 10 Hz) to a mouse hind paw. Their findings indicated that there is very fast neuromechanical coupling that responds in the 100 ms range which is valuable for BCI, because BCI has to respond to brain activity as quickly as possible. The shortcoming of fMRE is that it has relatively low spatiotemporal resolution and is expensive and not portable.

Shear wave elastography imaging (SWE) is an ultrasound modality that has much more attractive spatiotemporal characteristics than fMRE, is portable, less costly. SWE characterizes the elasticity of the medium by detecting the shear wave propagation speed in the medium and is applied in diagnosis of breast cancer [9], liver fibrosis [10], cardiac pathology [11], and musculoskeletal pathology [12]. Due to the recent finding of a neuromechanical coupling by Patz et al, SWE can measures the elasticity change of brain tissue that has a very fast response to the brain activities and has potential to be applied as a imaging mode for BCI. Shear waves can be generated by an ultrasound probe by transmitting a focused wave, and the resulting shear wave can be tracked by ultrafast ultrasound imaging. However, currently it is not possible to generate a shear wave in the brain, due to the presence of the skull. Speed of sound (SOS) through the human skull is faster than it does in the human brain tissue [13], and the wave is refracted when it penetrates the interfaces between soft tissue and skull, shown as Fig.1, which disable the energy to focus on the tissue area of interest. Therefore, like fUS, the application of SWE in the neuroscience is also currently limited by skull bones and requires a craniotomy [14].

Renaud et al. [15] imaged the bone cortex through a periosteum interface by implementing an aberration correction algorithm. Inspired by bone cortex imaging, this project also applied an aberration correction algorithm to the Transcranial SWE, which allows SWE measures the brain tissue stiffness noninvasively. There are two steps in SWE, (1) the shear wave generation by sending a focused wave, and (2) the shear wave readout by ultrafast imaging. Both steps are influenced by skull refraction. In this paper we propose to apply the aberration correction algorithm to correct for the refraction in both the shear wave generation (aberration pushing correction) and shear wave readout (aberration imaging correction).

II. MATERIAL AND METHOD

One simulation and three ex-vivo experiment were conducted to verify effectiveness of aberration pushing and imaging correction. The simulation experiment was performed by K-Wave simulation and divided into three parts to show how aberrator disturb the shear wave generation, and whether aberration correction can refocus the energy to generate
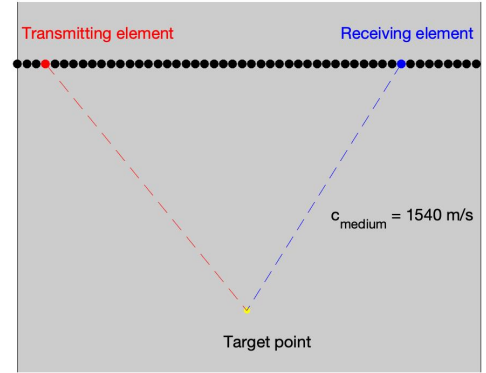
(a) Homogeneous medium.
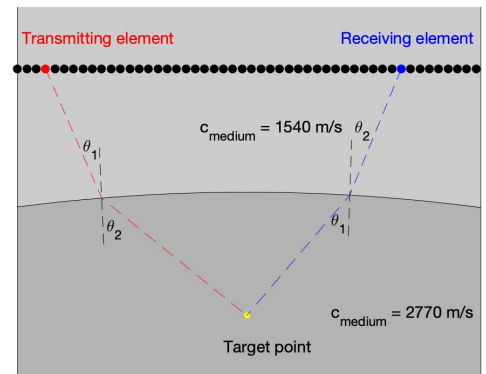
(b) Heterogeneous medium.

FIGURE 1: Two figures show the ultrasound beam path transmitted from the transmitting element (red) to the target point (yellow) and scattered from the target point (yellow) to the receiving element (blue). In the homogeneous medium, the ultrasound beam travels in a straight path (a), and in the heterogeneous medium, the ultrasound beam is refracted when it is through the interface between two mediums with different SOS (b). The incident angle θ_1 and refracted angle $theta_2$ obey Snell's law.

shear wave at the target location. (1) The first simulation pushes with parabolic delay to the homogeneous medium. (2) The second experiment pushes with parabolic delay to the heterogeneous medium. (3) The third experiment pushes with delay corrected by the aberration pushing correction to the heterogeneous medium.

The first ex-vivo experiment tested the performance of aberration correction on transcranial imaging by scanning the agar phantom with wire in it and includes 2 scans. (1) Image B-mode of the agar wire phantom without PVC slab at the top as a ground truth. (2) Image the B-mode of agar wire phantom with PVC slab at the top.

The second ex-vivo experiment including three shear wave

pushing and imaging processes tested the performance of aberration pushing correction. (1) Image the shear wave induced by pushing with the parabolic delay on the agar phantom without PVC slab. (2) Image the shear wave induced by push with the parabolic delay on the agar phantom with PVC slab. (3) Image the shear wave induced by pushing with the delay corrected by the aberration pushing correction on the agar phantom with PVC slab.

The third experiment was conducted on the another agar phantom that has inclusions and a PVC slab. This experiment tested if, with aberration imaging and pushing correction, we are able to reconstruct the elasticity of the phantom with an aberrator between probe and tissue so that can achieve transcranial functional shear wave elastography.

A. ABERRATION PUSHING CORRECTION

In order to generate a shear wave, a focused beam must be generated by the ultrasound probe, which is generated by delaying the ultrasound pulse transmitting from different transducers (The physics behind shear wave generation is referred in Appendix A). The delay is obtained by calculating the time difference between transducers to the target point and enables the ultrasound beam from every transducer arrives at the target point simultaneously. In the homogeneous medium, the focused beam delay is usually parabolic, and is displayed as the virtual position of transducers in Fig. 2a. However, for transcranial imaging, the medium is heterogeneous, because the SOS is around 2770 m/s in skull layer and 1540 m/s in brain tissue. In the heterogeneous medium, the travel time for ultrasound beam from transducers to the target point is altered by refraction, and the ultrasound beam from transducers can not reach the target point simultaneously with the parabolic delay used for push in the homogeneous medium. Fig. 2b depicts that with the same pushing delay, the ray path has unequal length and travel time for every transducer in the heterogeneous medium, which results in the unfocused beam. Unfocused beam push might cause the dispersion of acoustic radiation energy, weakening the shear wave amplitude, reducing the shear wave tracking quality, and generating the shear wave at the wrong location.

To refocus the ultrasound beam, this project adjusts the pushing delay with the aberration pushing correction based upon the ray tracing algorithm (The ray tracing algorithm is described in Appendix D). To obtain the correct ultrasound beam path, the ray tracing algorithm needs a precise segmentation of interfaces and an accurate estimate of SOS of the medium. The segmentation algorithm seeks the shortest path that follows the interface with the highest intensity in the ultrasound image and fits the segmentation line with polynomial regression [16]. The SOS measurement is done by an auto-focus algorithm that searches for the best quality image reconstructed by the SOS within a relevant range [17]. With the corrected ultrasound beam path, the travel time of the ultrasound beam from transducers to the target point is corrected, shown as red solid line in Fig. 17c. The new pushing delay is obtained by calculating the corrected travel

time difference between transducers to the target point and ensures all ultrasound beam paths have the identical travel time. This project will certifies whether aberration pushing correction can refocus the ultrasound beam on the target point.

B. ABERRATION IMAGING CORRECTION

The shear wave is imaged by ultrafast ultrasound imaging technique after being induced in the medium. Ultrafast ultrasound imaging transmits the plane wave or diverging wave [18], and the received echoes are beamformed to images using Delay and Sum (DAS) beamforming to I/Q demodulated images. The ultrasound images of the shear wave can be processed to Tissue Doppler Images (TDI) using a one lag autocorrelation [19] method, and will contain the information of the tissue movement (The detail of Image reconstruction is referred in Appendix B).

As mentioned above, the reconstruction of ultrafast ultrasound images relies on the DAS algorithm that highly depends on the travel time of ultrasound beams. The correction of travel time for image reconstruction in the heterogeneous medium is achieved by the aberration imaging correction algorithm that is also based on the ray tracing algorithm. Like aberration pushing correction, the aberration imaging recalculates the ray path and travel time for ultrasound beam. The tiny difference is that the correction for shear wave push only need one-way ray path (from one of transducers to the target), and the correction for the image reconstruction requires round-trip ray path (from one of transducers to the target, and back to one of transducers) instead. With the corrected travel time provided by aberration imaging correction algorithm, DAS algorithm can correct the ultrasound images which are distorted by aberrator such as a skull by taking into account the refraction.

C. PHANTOM PREPARATION

The experiment was performed on two agar phantoms. The first agar phantom has 0.5% agar, is mixed with silicon carbide (0.2%) acting as scattering background particles, and contains a wire phantom. The second agar phantoms contain agar with four different concentrations. The background is formed with 0.5% of agar, and three cylindrical inclusions have 0.75%, 1%, and 1.5% of agar. Whole agar phantom is mixed with 0.2% silicon carbide. Boxes contain both phantoms with the size of ($7cm \times 7cm \times 8cm$) with absorbing material at the bottom. A 2.5 mm thick curved Polyvinyl chloride (PVC) slab which has a different SOS (2350 m/s) than agar phantom (1461 m/s that is calculated by autofocus algorithm) does, is prepared to act as an aberrator by being put on the surface of agar phantom and submersed in water.

D. TRANSCRANICAL FUNCTIONAL SHEAR WAVE SEQUENCE SETUP

Three experiments were performed on two agar phantoms and all were conducted with The Philips ATL ultrasound
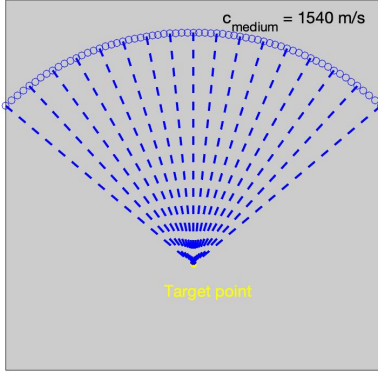
(a) Homogeneous medium.
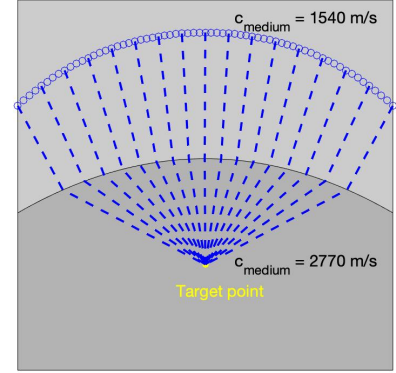
(b) heterogeneous medium.

FIGURE 2: Two figures show that focus beam push with parabola delay in the homogeneous medium and heterogeneous medium. The blue circle indicates the virtual position of transducers, yellow circle is the target point, and blue dash lines indicate the ultrasound beam path from transducers to target point.

probe linear L7-4 that contains 128 channels connected to the programmable ultrasound scanner (Verasonics Vantage, Seattle, USA). For imaging, we transmitted angled ultrasound plane waves ($-10 : 10 : 10°$) at a 16.5 kHz frame rate, which resulted in a 5.5 kHz frame rate after coherent compounding. The frequency of transmission is 5.208 MHz and the number of imaging pulse cycles is 2. The shear wave was generated at the expected depth of 19.64 mm by 64 transducer elements transmitting 1000 cycles pulse with a frequency of 5.208 MHz. In general, the transcranial functional shear wave sequence has five steps: (1) B-mode imaging. (2) Aberration correction based on the B-mode image to acquire the travel time. (3) Shear wave generation with pushing delay obtained by aberration pushing correction. (4) Shear wave imaging with aberration imaging correction. (5) Post data processing.

E. K-WAVE SIMULATION

The simulation experiment is simulated with the K-wave MATLAB toolbox (http://www.k-wave.org) [20]. For all simulations, the number of pushing elements is 96. The homogeneous medium has SOS of 1540 m/s, and The heterogeneous medium includes the aberrator with SOS of 2350 m/s. The position of the aberrator is shown in Fig. 3, and the SOS of background is still 1540 m/s. The result will be presented as energy field image extracted by taking maximum amplitude of each pixel in the time range of wave propagation.

F. POST DATA PROCESSING

The TDI data is filtered by a median filter (4×4) to remove the speckle noise. The evaluation of the B-mode image in the first experiment is by calculating the full width half max (FWHM) of the wire. The evaluation of the shear wave images is through two matrices: contrast, and SNR. The
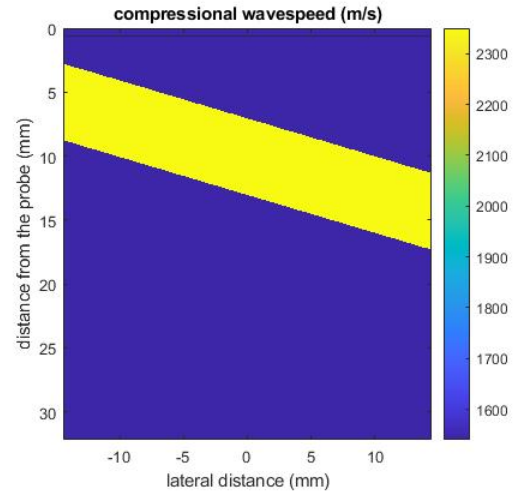

FIGURE 3: The structure of the heterogeneous medium that has soft medium with SOS of 1540 m/s (dark blue) and hard medium with SOS of 2350 m/s (yellow).

Contrast is calculated by:

$$\text{Contrast} = 10\log\frac{Signal_{in}}{Signal_{out}} \qquad (1)$$

where $Signal\_in$ is the signal of the shear wave which is obtained by averaging the square of pixel values in the ROI_{in}, $Signal\_in$ is the signal of the background which is obtained by the average the square of pixel values in the ROI_{out}. The positions of ROI_{in} and ROI_{out} are shown in Fig. 4.

Signal to noise ratio(SNR) is calculated by:

$$SNR = 10\log\frac{Signal_{in}}{Noise_{out}} \qquad (2)$$
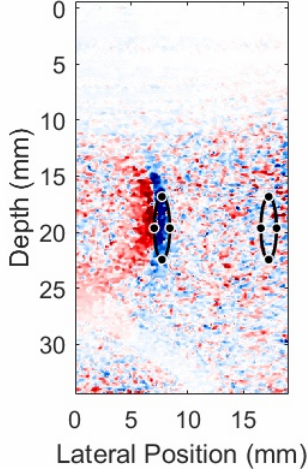
FIGURE 4: The shear wave image with ROI_{in} (Left ellipse on the shear wave) and ROI_{out} (Right ellipse)

where $Noise_{out}$ is the noise of the background which is obtained by the standard deviation of the square of pixel values in the $Noise_{out}$.

For the third experiment, the elasticity of agar phantom is reconstructed by time to peak method (TTP) (Other methods will be referred in Appendix C). TTP locates the position of shear wave front by determining the peak in the lateral direction for every imaging depth. For every imaging depth, a curve which indicates the shear wave location can be plotted as a function of time and can be converted to the speed by linear regression and first order time derivative. Finally, the elasticity of the medium is obtained by [21]:

$$E \approx 3\rho c^2 \tag{3}$$

where ρ is the density of medium, and c is the speed of shear wave in the medium.

III. RESULT
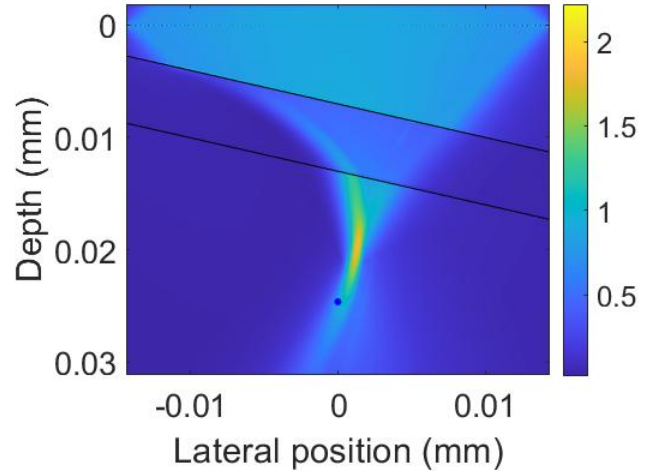
A. K-WAVE SIMULATION

Results of K-wave simulation are shown in Fig. 5. By pushing with parabolic, the energy field is generated around the target point in the homogeneous medium, shown in Fig. 5a. The PVC slab inserted in between the probe and the phantom refracts the ultrasound beam and allows it to focus on the higher location, shown in Fig. 5b. The focusing field is more dispersed and weaker than that generated in the homogeneous medium. After applying pushing aberration correction, the energy is refocused on the target point and more concentrated, but the the energy is still lost due to reflections at interfaces.

B. B MODE ON AGAR WIRE PHANTOM

In the result of agar wire phantom imaging shows the aberration imaging correction algorithm corrects the sound aberration caused by PVC slab. Fig. 6a shows the B-mode
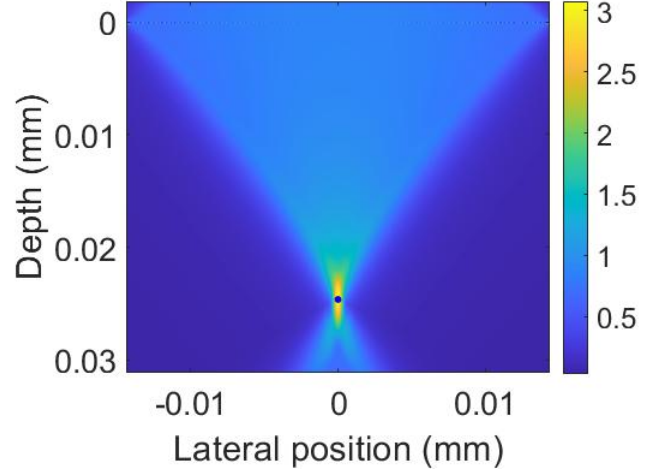
(a) Energy field generated in the homogeneous medium by pushing with parabolic delay.

(b) Energy field generated in the heterogeneous medium by pushing with parabolic delay.
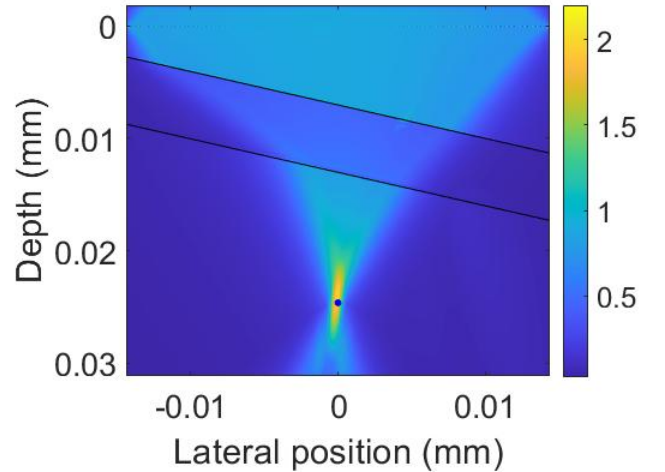
(c) Energy field generated in the heterogeneous medium by pushing with the delay corrected by aberration correction.

FIGURE 5: Results of three simulations presented as energy field, the black lines show the interfaces of aberrator.

image of agar wire phantom without PVC slab, and FWHM of the top wire is 0.40 mm and FWHM of the bottom wire is 0.44 mm. When adding the PVC slab in between the probe and the phantom, the B-mode image of agar wire phantom is distorted, shown in Fig. 6b. FWHM of the top wire is 0.63 mm and FWHM of the bottom wire is 1.2 mm. Wires in Fig. 6b move up a bit compared with Fig. 6a because assumed travel time is longer than the real travel time. By applying aberration imaging correction algorithm, the B-mode image is restored, shown in Fig. 6c. FWHM of the top wire is 0.43 mm and FWHM of the bottom wire is 0.47 mm. Locations of wires return to their original location in Fig. 6c. In Fig. 6b and Fig. 6c, two bright white lines at the top are interfaces of the PVC slab, which are expected. White lines further down are artifact caused by multiple reflections.

C. SHEAR WAVE MOVIE ON AGAR WIRE PHANTOM

The result of the second experiment is shown in Fig. 7. without aberrator present, the push with parabolic delay generates a strong shear wave whose center is around the expected focusing depth, as shown in Fig. 7a. In Fig. 7b, the PVC slab refracts the pushing beam and results in the weaker shear wave. The center of the shear wave is above the expected depth, which is in agreement with the result of simulation. Fig. 7c shows that the center of shear wave generated by pushing with delay corrected by aberration pushing correction matches the expected focusing depth and has higher amplitude than the shear wave in Fig. 7b.

The analysis of contrast and SNR, shown in Fig. 8, indicates that the aberration pushing correction algorithm increased the contrast and SNR of the shear wave images in general. In addition, the SNR and contrast of shear wave images degrade as shear wave propagates. Shear waves induced by the ultrasound beam pushed through the PVC slab has lower amplitude and attenuates more quickly than that is generated in the homogeneous medium, even though the push correction algorithm is applied.

D. ELASTICITY RECONSTRUCTION ON AGAR PHANTOM

The slope of shear wave trajectory in Fig. 10 indicates the speed of shear wave propagation, and the shear wave speed is converted to elasticity by Eq. 3. The elasticity of the inclusion with the agar concentration 1% in Fig. 9 is 209.5 kPa Young's modulus and the elasticity of the background is 24.2 kPa Young's modulus. The result shows that even with the aberrator, the aberration correction algorithm can still help SWE to measure the elasticity of the medium. In addition, the result indicates that the elasticity of agar medium increase as the concentration of agar increase.

IV. DISCUSSION

SWE is a potential neuroimaging modality because it is relatively low cost, portable, and has a high spatiotemporal resolution, but it but is currently invasive due to skull aberrations. This project proposes to use an aberration correction algorithm to correct aberration that occurs in both shear wave imaging and shear wave generation, and enable SWE to be a noninvasive neuroimaging modality.

For the imaging part, the result of qualities of images referred as FWHM of wires in Fig 6 prove that the aberration imaging correction algorithm is able to correct the distortion induced by PVC slab for B-mode imaging. However, unexpected multiple reflections not only can affect B-mode imaging but also can disturb the shear wave imaging. The aberration correction can't remove artifact induced by multiple reflections, because aberration correction can only fix the travel time due to the refraction. To remove multiple reflections, the tissue harmonic imaging can be applied in the future. Tissue harmonic imaging can acquire the non-linear ultrasound signal which has a hybrid frequency component. Since most multiple reflections are mainly in fundamental frequency [22], by filtering out fundamental frequency components, the harmonic imaging is able to remove multiple reflections. But harmonic imaging also has drawbacks that could reduce the imaging frame rate which is also crucial for SWE. The new technique, such as Ultrafast Harmonic Coherent Compound [23], can perform harmonic imaging without sacrificing the frame rate. But the trade-off between image quality and frame rate has to be made per applications.

In the shear wave generation part, the simulation shows the aberration pushing correction can refocus the energy at the target point, but can't prevent the loss of the energy due to multiple reflections at PVC slab interfaces. In the ex-vivo experiment, the shear wave generated by pushing with the corrected delay refocuses at the target point. However, the peak amplitude of the shear wave in Fig. 7c generated by the pushing correction is not fully restored compared with the shear wave in Fig. 7a. So, results of shear wave imaging on the phantom are consistent with the simulation.

Another interesting observation in the simulated aberration corrected shear wave push, is that the focusing field is rotated by the refraction at interfaces. The rotation of the energy field might lead to the rotation of the shear wave propagation, although the rotation of the shear wave propagation is not clearly seen in the ex-vivo experiment. The reason might be that the position of aberrator is not left-right symmetric in the simulation experiment, but aberration is basically symmetric in the ex-vivo experiment. In order to identify whether there is a rotation of the shear wave propagation and investigate the direction in a 2D plane, 2-D shear wave speed calculation and multi-directional filtering can be applied [24] in the future work. Some new shear wave tracking methods such as artificial intelligence [25] can be applied, which can potentially help the elasticity reconstruction.

The reconstruction of the medium elasticity with aberrator such as a PVC slab can be achieved by aberration correction.
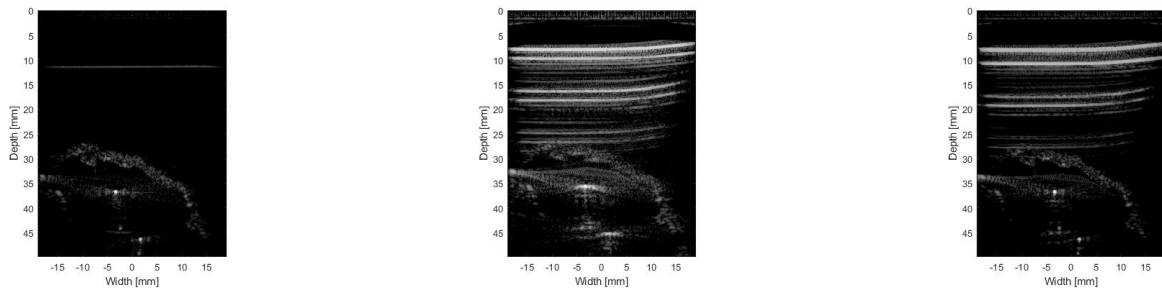
(a) B-mode image of agar wire phantom without PVC slab above it.

(b) B-mode image of agar wire phantom with PVC slab above it.

(c) B-mode image of agar wire phantom with PVC slab above it and corrected by aberration correction algorithm.

FIGURE 6: B-mode images of agar wire phantoms. The top wire is the bright dot at depth 37 mm, and the bottom wire is anther bright dot at the depth of 46 mm.

Unfortunately, the trajectory only covers the lateral position from -12 mm to 12 mm, because the SNR of the shear wave images degrades due to dispersion and attenuation as the shear wave propagates. The range of elasticity reconstruction area is limited by the amplitude of the shear wave. The pushing correction can't fully restore the energy loss due to multiple reflections, thus, it requires a longer ultrasound pulse or more pushing transducer elements to generate stronger shear waves through the skull. That might raise concerns about the brain health. The absence of harmful effects by SWE during studies conducted on an animal model such as baboons would allow us to state that its risk of heating and cavitation, within the regulatory energy limits, do not differ from other ultrasound imaging modalities. [26]. Even so, the risks remains to be quantified in ex-vivo, before the increase of energy applied to generate higher peak amplitude shear waves. Another solution for limitation of the SWE imaging area is shear wave compounding by generating the shear wave at multiple locations [27] or with multiple angles [24].

The application of transcranial functional SWE in BCI still has some challenges. The scanning rate of the elasticity map is about $8ms$ which is close to the EEG excluding the computational time consuming. But the time spend on the post data processing could reduce the scanning rate. So to increase the temporal resolution of SWE, the post data processing such as beam-forming or elasticity map recovery algorithm can be optimized. Another challenge is limited spatial solution which is related to the frame rate of ultrasound imaging and wavelength of the shear wave. So more optimization of spatial resolution such as increasing the imaging frame rate is required for transcranial functional SWE.

In Fig. 7b, it shows that the shear wave still can be generated even through the PVC slab. The reason might be that the refraction of PVC slab is not strong enough. In order to make our in ex-vivo experiment closer to the real application scenario, the aberration correction can be tested with the bone mimicking material that can mimic skull thickness and anisotropy [28] acting as the aberrating layer in the ex-vivo experiment. The in-vivo experiment of the transcranial functional SWE can be tested on large animals. The challenge for the small animal experiment is that it requires a smaller probe with a higher frequency that might be difficult to generate large energy to excite shear waves. So for the in-vivo experiment, a large animal is suggested.

In general, with the aberration correction algorithm, the transcranial SWE is achievable in a certain range of area size, and it can be applied to the diagnosis of brain disease. But due to the limitation of spatial resolution, temporal resolution, and the lack of research on neuromechanical couplings, the application of transcranial functional SWE in BCI still requires more in-vivo experiments.

V. CONCLUSION

This project proves that the aberration imaging correction and pushing correction can increase the quality of shear wave images, which can help achieve SWE transcranially. Although transcranial functional SWE still has weakness in spatial range of measurements, temporal resolution, and spatial resolution, it has the potential to be applied to BCI as the development of shear wave tracking technique and high frame rate ultrasound imaging.

REFERENCES

[1] A. J. Lui and N. N. Byl, "A systematic review of the effect of moderate intensity exercise on function and disease progression in amyotrophic lateral sclerosis," Journal of Neurologic Physical Therapy, vol. 33, no. 2, pp. 68–87, 2009.

[2] D. P. Nowlis and J. Kamiya, "The control of electroencephalographic alpha rhythms through auditory feedback and the associated mental activity," Psychophysiology, vol. 6, no. 4, pp. 476–484, 1970.

[3] M. Akhtari, H. Bryant, A. Mamelak, L. Heller, J. Shih, M. Mandelkern, A. Matlachov, D. Ranken, E. Best, and W. Sutherling, "Conductivities of three-layer human skull," Brain Topography, vol. 13, no. 1, pp. 29–42, 2000.

[4] L. R. Hochberg, M. D. Serruya, G. M. Friehs, J. A. Mukand, M. Saleh, A. H. Caplan, A. Branner, D. Chen, R. D. Penn, and J. P. Donoghue, "Neuronal ensemble control of prosthetic devices by a human with tetraplegia," Nature, vol. 442, no. 7099, pp. 164–171, 2006.

[5] J. Mellinger, G. Schalk, C. Braun, H. Preissl, W. Rosenstiel, N. Birbaumer, and A. Kübler, "An meg-based brain–computer interface (bci)," Neuroimage, vol. 36, no. 3, pp. 581–593, 2007.
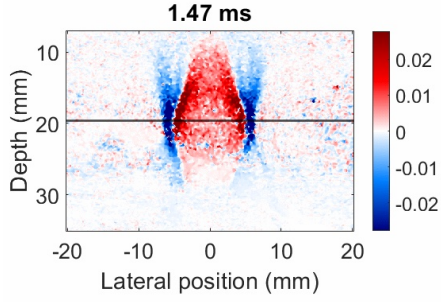
(a) Image of shear wave in the agar wire phantom without PVC slab above it, and the shear wave is generated by the push with parabolic delay.
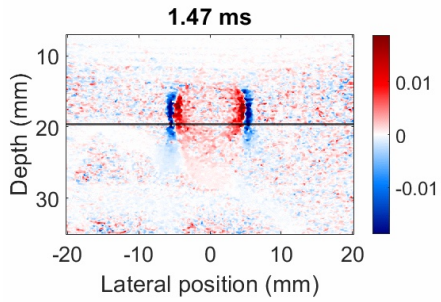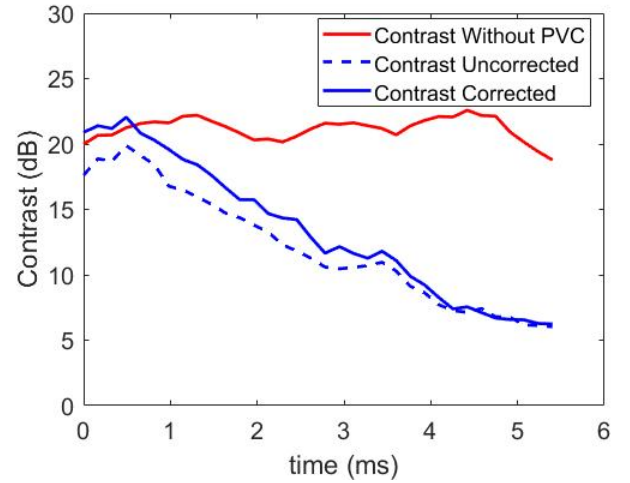

(b) Image of shear wave in the agar wire phantom with PVC slab above it, and the shear wave is generated by the push with parabolic delay.
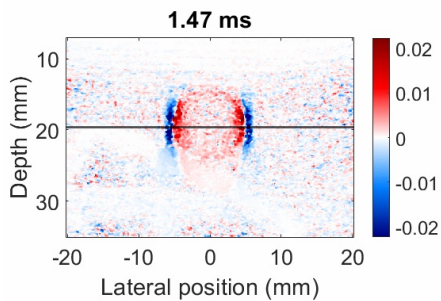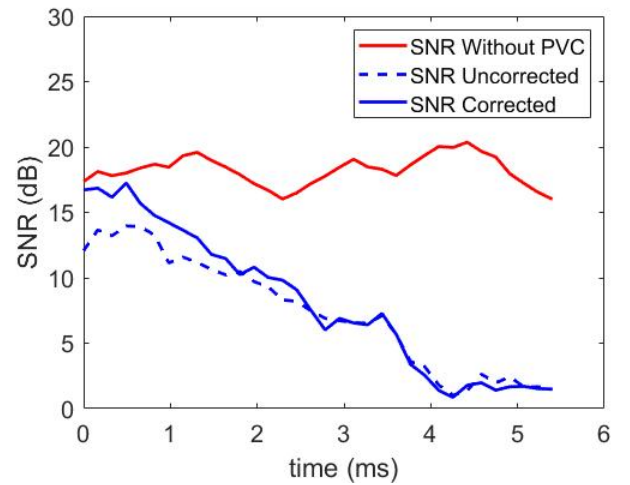

(c) Image of shear wave in the agar wire phantom with PVC slab above it and the shear wave is generated by the push with delay corrected by aberration correction.

FIGURE 7: Images of shear wave in agar wire phantoms. Images are extracted $1.47\ ms$ after recording shear wave. The black line is expected focusing depth ($19.7\ mm$) which is also the expected shear wave center.

(a) The contrast of shear wave images as a function of the time. The average contrast is $21.1\pm1.7\ dB$ for shear wave generated by pushing with parabolic delay in the agar wire phantom without PVC slab (Red line). The average contrast is $12.0\pm4.8\ dB$ for shear wave generated by pushing with parabolic delay in the agar wire phantom with PVC slab (blue dash line). The average contrast is $13.4\pm5.6\ dB$ for shear wave generated by pushing with corrected delay in the agar wire phantom with PVC slab (blue solid line).

(b) The SNR of shear wave images as a function of the time. The average SNR is $18.2\pm2.2\ dB$ for shear wave generated by pushing with parabolic delay in the agar wire phantom without PVC slab (Red line). The average SNR is $7.35\pm5.0\ dB$ for shear wave generated by pushing with parabolic delay in the agar wire phantom with PVC slab (blue dash line). The average SNR is $8.1\pm6.1\ dB$ for shear wave generated by pushing with corrected delay in the agar wire phantom with PVC slab (blue solid line).

FIGURE 8: The contrast ans SNR of shear wave images that is plotted as a function of time.

[6] E. Macé, G. Montaldo, I. Cohen, M. Baulac, M. Fink, and M. Tanter, "Functional ultrasound imaging of the brain," Nature methods, vol. 8, no. 8, pp. 662–664, 2011.

[7] A.-K. Aydin, W. D. Haselden, Y. Goulam Houssen, C. Pouzat, R. L. Rungta, C. Demené, M. Tanter, P. J. Drew, S. Charpak, and D. Boido, "Transfer functions linking neural calcium to single voxel functional ultrasound signal," Nature communications, vol. 11, no. 1, pp. 1–10, 2020.

[8] S. Patz, D. Fovargue, K. Schregel, N. Nazari, M. Palotai, P. E. Barbone,
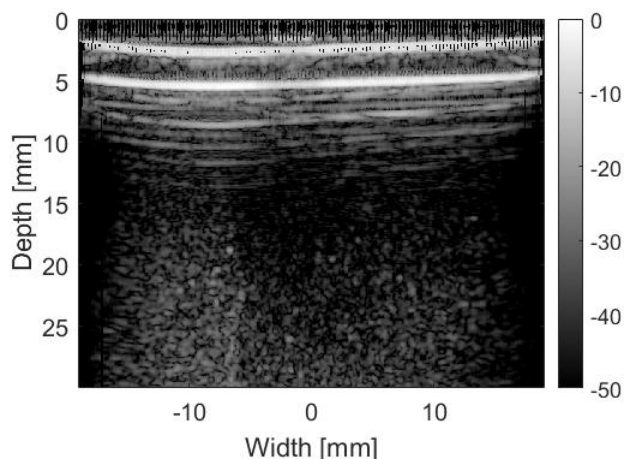
FIGURE 9: The B-mode image of the agar phantom for elasticity reconstruction. The inclusion with agar concentration of 1% is between the red line is t, and the background with agar concentration of 0.5% is beyond the red line.
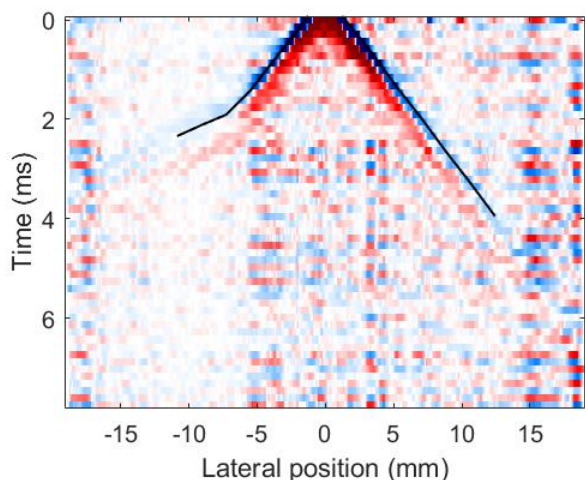

FIGURE 10: M-mode of TDI at the depth of 19.64 mm where is the focusing depth. The trajectory of the shear wave (black line) is extracted by TTP algorithm.

B. Fabry, A. Hammers, S. Holm, S. Kozerke, et al., "Imaging localized neuronal activity at fast time scales through biomechanics," Science advances, vol. 5, no. 4, p. eaav3816, 2019.

[9] B. Liu, Y. Zheng, G. Huang, M. Lin, Q. Shan, Y. Lu, W. Tian, and X. Xie, "Breast lesions: quantitative diagnosis using ultrasound shear wave elastography—a systematic review and meta-analysis," Ultrasound in medicine & biology, vol. 42, no. 4, pp. 835–847, 2016.

[10] G. Ferraioli, P. Parekh, A. B. Levitov, and C. Filice, "Shear wave elastography for evaluation of liver fibrosis," Journal of Ultrasound in Medicine, vol. 33, no. 2, pp. 197–203, 2014.

[11] A. Caenen, M. Pernot, K. R. Nightingale, J.-U. Voigt, H. J. Vos, P. Segers, and J. D'hooge, "Assessing cardiac stiffness using ultrasound shear wave elastography," Physics in Medicine & Biology, vol. 67, no. 2, p. 02TR01, 2022.

[12] M. S. Taljanovic, L. H. Gimber, G. W. Becker, L. D. Latt, A. S. Klauser, D. M. Melville, L. Gao, and R. S. Witte, "Shear-wave elastography: basic physics and musculoskeletal applications," Radiographics, vol. 37, no. 3,

p. 855, 2017.

[13] F. A. Duck, Physical properties of tissues: a comprehensive reference book. Academic press, 2013.

[14] D. Chauvet, M. Imbault, L. Capelle, C. Demene, C. Karachi, A.-L. Boch, J.-L. Gennisson, and M. Tanter, "In vivo measurement of brain tumor elasticity using intraoperative shear wave elastography," Ultraschall in der Medizin-European Journal of Ultrasound, vol. 37, no. 06, pp. 584–590, 2016.

[15] G. Renaud, P. Kruizinga, D. Cassereau, and P. Laugier, "In vivo ultrasound imaging of the bone cortex," Physics in Medicine & Biology, vol. 63, no. 12, p. 125010, 2018.

[16] D. Hong, "Medical image segmentation based on accelerated dijkstra algorithm," in Advances in Intelligent Systems, pp. 341–348, Springer, 2012.

[17] B. E. Treeby, T. K. Varslot, E. Z. Zhang, J. G. Laufer, and P. C. Beard, "Automatic sound speed selection in photoacoustic image reconstruction using an autofocus approach," Journal of biomedical optics, vol. 16, no. 9, p. 090501, 2011.

[18] G. R. Lockwood, J. R. Talman, and S. S. Brunke, "Real-time 3-d ultrasound imaging using sparse synthetic aperture beamforming," IEEE transactions on ultrasonics, ferroelectrics, and frequency control, vol. 45, no. 4, pp. 980–988, 1998.

[19] B. Brekke, L. C. Nilsen, J. Lund, H. Torp, T. Bjastad, B. H. Amundsen, A. Stoylen, and S. A. Aase, "Ultra-high frame rate tissue doppler imaging," Ultrasound in medicine & biology, vol. 40, no. 1, pp. 222–231, 2014.

[20] B. E. Treeby and B. T. Cox, "k-wave: Matlab toolbox for the simulation and reconstruction of photoacoustic wave fields," Journal of biomedical optics, vol. 15, no. 2, p. 021314, 2010.

[21] H. J. Vos, B. M. van Dalen, I. Heinonen, J. G. Bosch, O. Sorop, D. J. Duncker, A. F. van der Steen, and N. de Jong, "Cardiac shear wave velocity detection in the porcine heart," Ultrasound in medicine & biology, vol. 43, no. 4, pp. 753–764, 2017.

[22] M. A. Averkiou, "Tissue harmonic imaging," in 2000 IEEE Ultrasonics Symposium. Proceedings. An International Symposium (Cat. No. 00CH37121), vol. 2, pp. 1563–1572, IEEE, 2000.

[23] M. Correia, J. Provost, S. Chatelin, O. Villemain, M. Tanter, and M. Pernot, "Ultrafast harmonic coherent compound (uhcc) imaging for high frame rate echocardiography and shear-wave elastography," IEEE transactions on ultrasonics, ferroelectrics, and frequency control, vol. 63, no. 3, pp. 420–431, 2016.

[24] P. Song, A. Manduca, H. Zhao, M. W. Urban, J. F. Greenleaf, and S. Chen, "Fast shear compounding using robust 2-d shear wave speed calculation and multi-directional filtering," Ultrasound in medicine & biology, vol. 40, no. 6, pp. 1343–1355, 2014.

[25] R. Delaunay, Y. Hu, and T. Vercauteren, "An unsupervised learning-based shear wave tracking method for ultrasound elastography," in Medical Imaging 2022: Ultrasonic Imaging and Tomography, vol. 12038, pp. 149–155, SPIE, 2022.

[26] M. Issaoui, A. Debost-Legrand, K. Skerl, B. Chauveau, B. Magnin, A. Delabaere, L. Boyer, M.-P. Sauvant-Rochat, and D. Lemery, "Shear wave elastography safety in fetus: a quantitative health risk assessment," Diagnostic and interventional imaging, vol. 99, no. 9, pp. 519–524, 2018.

[27] E. Macé, I. Cohen, G. Montaldo, R. Miles, M. Fink, and M. Tanter, "In vivo mapping of brain elasticity in small animals using shear wave imaging," IEEE transactions on medical imaging, vol. 30, no. 3, pp. 550–558, 2010.

[28] N. Chauveau, X. Franceries, B. Doyon, B. Rigaud, J. P. Morucci, and P. Celsis, "Effects of skull thickness, anisotropy, and inhomogeneity on forward eeg/erp computations using a spherical three-dimensional resistor mesh model," Human brain mapping, vol. 21, no. 2, pp. 86–97, 2004.

[29] G. Torr, "The acoustic radiation force," American Journal of Physics, vol. 52, no. 5, pp. 402–408, 1984.

[30] J. White, "Quantitative seismology, theory and methods volume i and volume ii by keiiti aki and paul g. richards," 1980.

[31] J. Bercoff, M. Tanter, and M. Fink, "Supersonic shear imaging: a new technique for soft tissue elasticity mapping," IEEE transactions on ultrasonics, ferroelectrics, and frequency control, vol. 51, no. 4, pp. 396–409, 2004.

[32] M. Tanter and M. Fink, "Ultrafast imaging in biomedical ultrasound," IEEE transactions on ultrasonics, ferroelectrics, and frequency control, vol. 61, no. 1, pp. 102–119, 2014.

[33] G. Montaldo, M. Tanter, J. Bercoff, N. Benech, and M. Fink, "Coherent plane-wave compounding for very high frame rate ultrasonography and transient elastography," IEEE transactions on ultrasonics, ferroelectrics, and frequency control, vol. 56, no. 3, pp. 489–506, 2009.

[34] N. C. Rouze, M. H. Wang, M. L. Palmeri, and K. R. Nightingale, "Parameters affecting the resolution and accuracy of 2-d quantitative shear wave images," IEEE transactions on ultrasonics, ferroelectrics, and frequency control, vol. 59, no. 8, pp. 1729–1740, 2012.

[35] M. Born, "E wolf principles of optics chl," 1959.

[36] D. Waltham, "Two-point ray tracing using fermat's principle," Geophysical Journal International, vol. 93, no. 3, pp. 575–582, 1988.

A. PHYSICS BEHIND GENERATING SHEAR WAVE BY FOCUSED BEAM

SWE maps the medium elasticity by measuring the shear wave speed in that medium. In this project, the shear wave is generated by the acoustic radiation force that is exerted by a sound wave generated by ultrasound transducers [29]. The acoustic radiation force is generally to write:

$$F(\vec{r}, t) = \frac{2\alpha I(\vec{r}, t)}{c} \tag{4}$$

where α indicates the ultrasound attenuation, I indicates the local intensity of the ultrasonic beam. and c indicates the sos in the medium. In the elastic medium, acoustic radiation force generate three mechanical waves: a compression wave $g_{ij}^p(\vec{r}, t)$, a shear wave $g_{ij}^s(\vec{r}, t)$, and a coupling term between compression wave and shear wave $g_{ij}^{ps}(\vec{r}, t)$ due to Green's function [30]:

$$g_{ij}(\vec{r}, t) = g_{ij}^p(\vec{r}, t) + g_{ij}^s(\vec{r}, t) + g_{ij}^{ps}(\vec{r}, t) \tag{5}$$

By focused beam, the acoustic radiation force is focused on the target tissue and applied longitudinally. Then the target tissue displaces longitudinally due to acoustic force. The longitudinal displacement mainly propagates transversely and has a bipolar directivity pattern [31], which is a form of the shear wave. The shear modulus of the medium is related to the speed of shear wave propagation and is calculated as [31]:

$$\mu = \rho c^2 \tag{6}$$

where μ indicates the shear modulus of the medium, ρ indicates the density of the medium, and c indicates the speed of the shear wave in the medium. Eq. 6 is an assumption as the medium in this project is assumed to be pure elastic. For the final result, the elasticity is quantified by Young's modulus which is estimated as [31]:

$$E = 3\mu \tag{7}$$

In respect of SWE, the focused beam is generated by tuning the delay of high amplitude ultrasound wave transmitting from transducers. For a single focused beam, the delay is parabola, shown as Fig. 11, and the form of the shear wave is shown as Fig. 13a.

In addition to the single focused beam, the supersonic shear wave is also generated by parabola delay pushes [31], but instead of one push, the supersonic shear wave is made up of multiple point sources which are induced sequentially along the beam axis. Fig. 13b shows that the supersonic shear wave has a much larger focal zone compared to the single-point source which can extend the area of the elasticity map.

Another way of pushing which can increase the length of the shear wave field is the Bessel beam by pushing with conical delay, shown as Fig. 12. Fig. 13c shows that the Bessel beam has a longer length of the field.
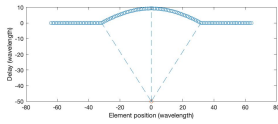
FIGURE 11: The shear wave pushes with parabola delay. The blue circle indicates the virtual position of transducers, and the red circle is the target point. The transducers with zero delays outside the blue dash line don't transmit ultrasound pulse. All blue dash lines have an identical length, which indicates that ultrasound beams from all the transducers reach the target point at the same time.
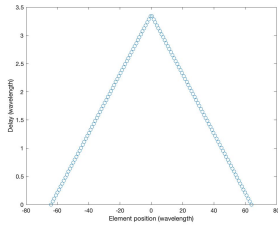

FIGURE 12: Shear wave push with conical delay. The blue circle indicates the virtual position of transducers.

B. SHEAR WAVE IMAGES RECONSTRUCTION

Shear wave images reconstruction takes two steps: data acquisition that is similar to the B-mode ultrasound acquisition, and tissue Doppler imaging (TDI) extraction.

Unlike B-mode data acquisition, a shear wave image requires a very high frame rate. The shear wave propagates in the human tissue at the speed of 1 to 10 m/s [5], and the width of the ultrasound image is less than 40 mm, which means it requires an imaging frame rate higher than 1000 frames per second (fps) to capture the shear wave before it propagates throughout the imaging range. However, The conventional ultrasonic imaging (line-by-line focused beams) can only reach $\sim$ 25 fps [32]. As a technological breakthrough, ultrafast ultrasound imaging that can achieve faster than 1000 fps was developed [32]. By transmitting the plane wave or diverging wave [18] that can propagate through the whole imaging area, ultrafast ultrasound imaging can acquire one frame of an image by a single transmitting, which increases the frame rate significantly.

When the plane wave hits the inclusion in the medium, the scattering wave is generated from the inclusion. The scattering waves travel back to the probe and are received by the elements. All the elements receive the wave continuously and form RF data, and RF data then is demodulated to IQ-demodulated data (IQ data). The amplitude of every point in RF data indicates the amplitude of the wave received by a receiver with the travel time which is from the transmitter to

a pixel in the medium and scattered back to the receiver. Then for every pixel in the medium, all the receivers can receive the scattering waveform of this pixel, but with different travel times. The intensity of a pixel is calculated by the sum of the amplitude of the scattering wave from this pixel received by all the receivers. Every receiver receives the scattering wave at a different time, so there are delays for different receivers to receive the scattering wave from the same pixel. Therefore, The algorithm which sums up the amplitude of different receivers is called Delay and Sum (DAS).

With single plane wave or diverging wave transmitting, ultrafast ultrasound imaging achieves a very high frame rate but result in a relatively low the signal to noise ratio (SNR) compared to conventional ultrasound imaging with line-by-line focused beams transmitting [32]. To obtain higher SNR images for SWE, coherent compounding [33] is implemented in this project to improve the image quality. Although coherent compounding scarifies the frame rate, the frame rate of imaging is still high enough to track the shear wave propagation.

The shear wave as mentioned in the last section is a form of target tissue longitudinal displacements which share a similar basis with TDI. For TDI, the local tissue displacements can be obtained by one-lag autocorrelation [19]. Therefore, the shear wave propagation in the tissue is displayed by TDI that can also be extracted by one-lag autocorrelation. With the DAS algorithm, Every frame was reconstructed to IQ data $S(x, z, i)$, where i is the frame number, x and z indicates the coordinates for every pixel. Then the TDI data $v(x, z, i)$ are calculate:

$$v(x, z, i) = \frac{\angle S(x, z, i) \cdot S^*(x, z, i-1)}{\pi} v_N \qquad (8)$$

$$v_N = \frac{\lambda F}{4} \qquad (9)$$

Where S is IQ data, i is the frame number, by taking the inner product between two adjacent frames, get the phase shift between the two frames. v_N is Nyquist velocity which is calculated by equation (9), where λ is the wavelength of pushing wave and F is frame rate. Three frames of the TDI data $v(x, z, i)$ are shown in Fig. 14.

C. ELASTICITY RECONSTRUCTION

To reconstruct the shear wave speed and elasticity, the time of flight(ToF) methods are implemented in this project. The ToF recovers the shear wave velocity which can be covert to the elasticity of the medium by formula [21]:

$$E \approx 3\rho c^2 \qquad (10)$$

where ρ is the density of medium, and c is the speed of shear wave in the medium.

To recover the shear wave propagation velocity, the Radon transform which is often used for line detection can provide the slope of the shear wavefront in the M-mode images, shown as Fig. [21]. The Radon transform takes the original

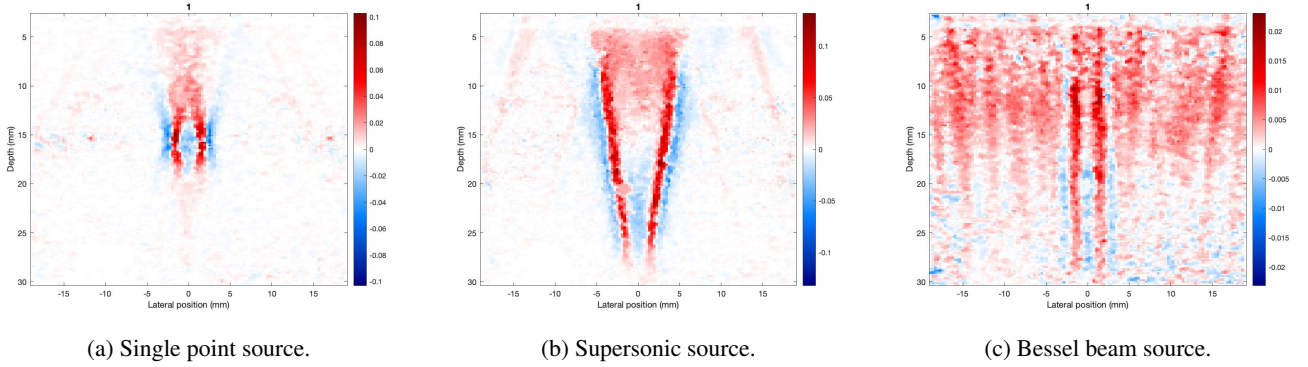(a) Single point source. (b) Supersonic source. (c) Bessel beam source.

FIGURE 13: The image of shear wave front generated by different sources. All those images are imaged in the CIRS phantom MODEL 040GSE. The red pixel with positive value indicates that the local tissue particle is moving upwards, and the blue pixel with positive value indicates that the local tissue particle is moving downwards.

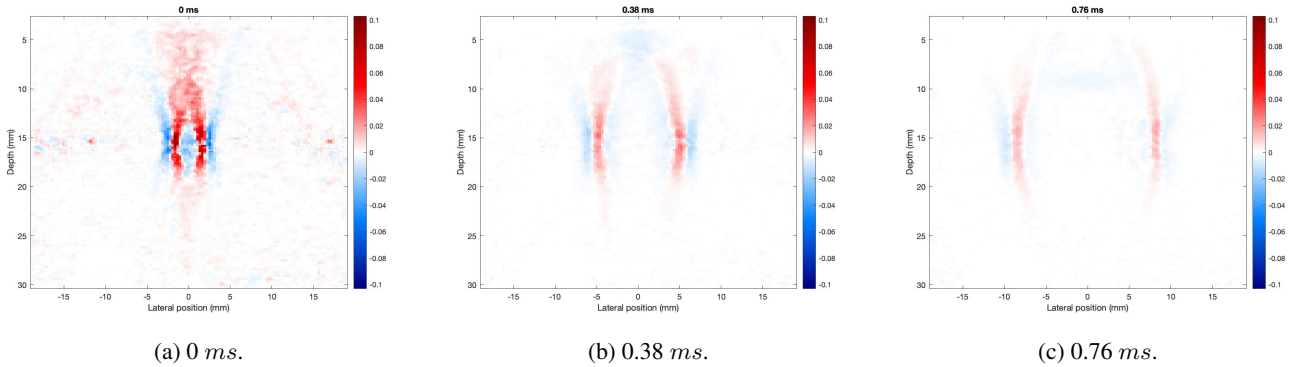(a) 0 ms. (b) 0.38 ms. (c) 0.76 ms.

FIGURE 14: The image of shear wave image at different sampling time. The shear wave was generated by single focused beam in the CIRS phantom MODEL 040GSE.

image which is in the spatial domain and transforms it into the Radon domain. The Radon domain is expressed in an angle coordinate and an intercept, and the Radon transform determines the integral over a line in the original image described by the angle and intercept. Therefore, a line through the peaks in the M-mode will show up with high intensity in the Radon domain The angle from the point in the Radon domain with the highest intensity is the slope of the shear wavefront and the slope can be converted to a shear wave propagation velocity.

The radon transform performs well with straight line detection, however, it does not perform well on the phantom with elastic inclusion. Some methods can trace the wavefront of a shear wave dynamically by determining the peak of shear wave (time to peak (TTP)), peak of derivative pf shear wave (time to peak slope (TTPS)), and displacement of shear wave relative to the previous frame (a lag position correlation(ALPC)) [34]. Combined with the line regression, the velocity can be obtain through the slope of the shear wave track.
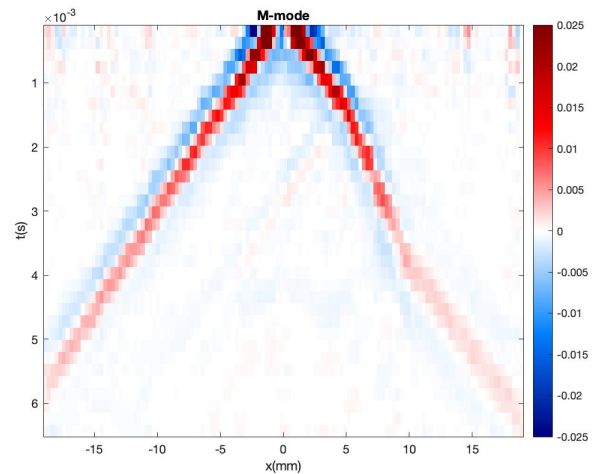

FIGURE 15: M-mode image that is extracted from TDI data Fig. 14 along the horizontal axis (parallel to the medium surface) at a certain depth and displayed as a function of time. The red trajectory indicates the shear wave propagation whose slope is the propagation velocity

D. RAY TRACING

In the heterogeneous medium, the ray path is bent, due to Snell's law:

$$\frac{sin\theta_1}{sin\theta_2} = \frac{v_1}{v_2} \qquad (11)$$

where θ_1 is the angle of incidence, θ_2 is the angle of refraction, v_1 is the SOS in incident medium, and v_2 is the refracted medium [35]. In the heterogeneous, the travel path of ultrasound beam is bent as Fig. 1b.

However, in practical work, Snell's law approach is difficult and computationally expensive to achieve with multiple ray-paths and multiple interfaces [36]. Therefore, the calculation of the ray path is performed with a ray tracing algorithm which is based upon Fermat's principle that light travels between two points along the path that requires the least time, as compared to other nearby paths [36].

The two layers ray tracing algorithm based on Fermat's principle has three steps. Firstly, the algorithm lists all ray paths which are through the whole interface regardless of Snell's law, shown as Fig.16a. Secondly, the algorithm calculates the travel time for all tray-paths and plots them as a function of interface intersection position, shown as Fig 16b. Thirdly, the algorithm determines the stationary point with the correct interface intersection position in Fig. 16b. By plotting the ray path through the stationary point on the interface with the correct interface intersection position, the correct ray path that obeys Snell's law is obtained, shown in Fig. 16c.

For transcranial SWE imaging, the medium has three layers (tissue, skull, tissue) if ignoring the thickness of the lens thickness, where the ultrasound pulse interacts with two interfaces. Therefore, the correct ultrasound beam path in the three layers heterogeneous is obtained by implementing three layers ray tracing algorithm. Based on the two layers ray tracing algorithm, three layers ray tracing algorithm also searches for the shortest time ray path through interfaces by applying the stationary point searching iteration. The three layers ray tracing takes three steps. Firstly, find the ray path from the transducer to the second interface with two layer ray tracing algorithm and connect the target point in the third layer to the second interface, shown in Fig. 17a. Secondly, calculate the travel time for all tray-paths and plot them as a function of the second interface intersection position, shown as Fig. 17b. Thirdly, find the stationary point in Fig. 17c which determines the correct intersection position for both interfaces. The ray path through this intersection position has the least travel time and obeys Snell's law.

● ● ●

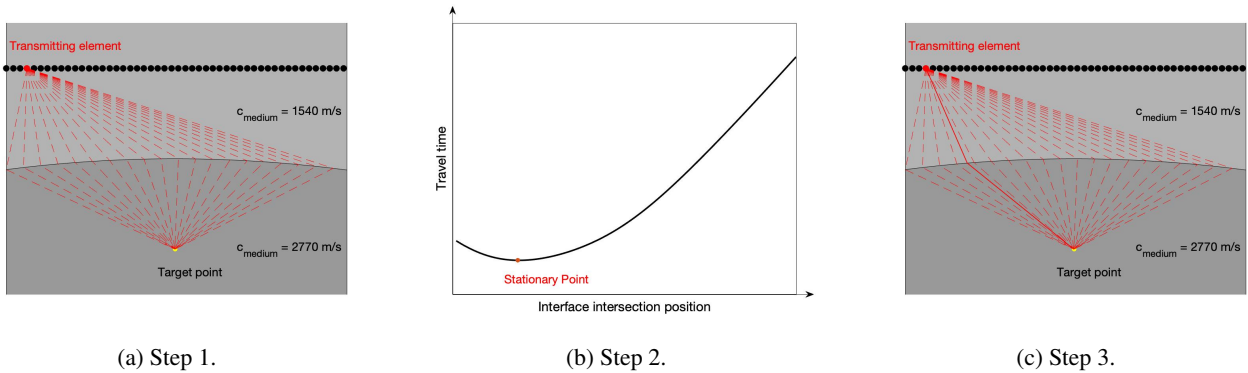(a) Step 1. (b) Step 2. (c) Step 3.

FIGURE 16: Three figures illustrate the process of ultrasound beam path determination through two layers of medium. The first step: determine all the ray path (red dash line) from transmitting element to the target point by removing the constraint of Snell's law, shown as Fig. 16a. The second step: Each of the resulting ray paths (red dash line) has an associated travel time which may be plotted as a function of interface intersection position, shown as Fig. 16b. The third step: search for the stationary point in Fig. 16b (red point) and plot the ray path through the interface with the correct interface intersection position. The correct ray path (red solid line) is shown in Fig. 16c.

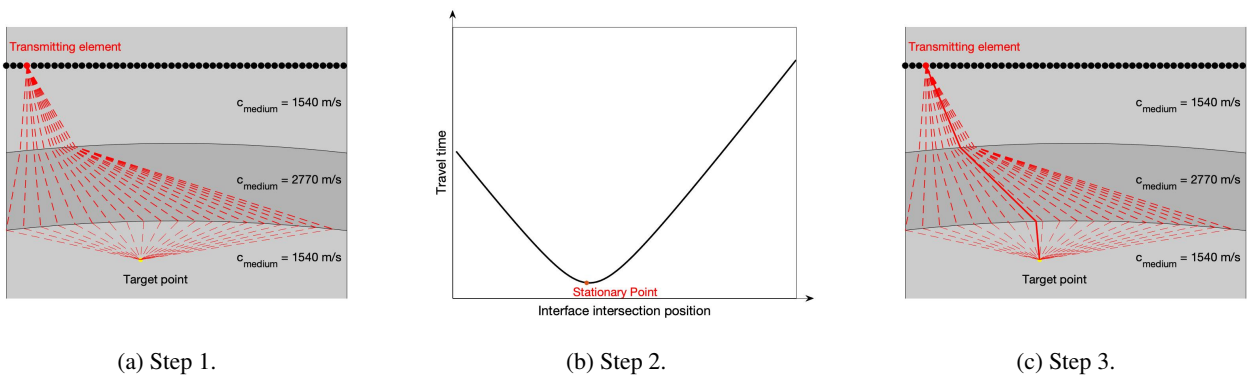(a) Step 1. (b) Step 2. (c) Step 3.

FIGURE 17: Three figures illustrate the process of ultrasound beam path determination through three layers of medium. The first step: determine all the ray path (red dash line) from transmitting elements to all points on the second interface by two layers ray tracing algorithm, and connect all points on the second interface to the target point, shown as Fig. 16a. The second step: Each of the resulting ray paths (red dash line) has an associated travel time which may be plotted as a function of the second interface intersection position, shown as Fig. 16b. The third step: search for the stationary point in Fig. 16b (red point) and plot the ray path through the second interface with the correct interface intersection position. The correct ray path (red solid line) is shown in Fig. 16c.